Deformation-induced Au precipitation kinetics in Fe-Au-W alloys studied by time-resolved small angle neutron scattering

Fu, Y.; Kohlbrecher, J.; Tichelaar, F. D.; Hendrikx, R. W.A.; Böttger, A. J.; Brück, E.; van der Zwaag, S.; van Dijk, N. H.

DOI
10.1016/j.mtla.2024.102322

Publication date
2025

Document Version
Final published version

Published in
Materialia

MTLA 39 (2025) 102322

Contents lists available at ScienceDirect

Materialia

journal homepage: www.elsevier.com/locate/mtla

Deformation-induced Au precipitation kinetics in Fe-Au-W alloys studied by time-resolved small angle neutron scattering

Y. Fu [a,b], J. Kohlbrecher [c], F.D. Tichelaar [d], R.W.A. Hendrikx [e], A.J. Böttger [e], E. Brück [a], S. van der Zwaag [b], N.H. van Dijk [a,*]

[a] Fundamental Aspects of Materials and Energy group, Faculty of Applied Sciences, Department of Radiation Science & Technology, Delft University of Technology, Mekelweg 15, Delft 2629 JB, the Netherlands
[b] Novel Aerospace Materials group, Faculty of Aerospace Engineering, Delft University of Technology, Kluyverweg 1, Delft 2629 HS, the Netherlands
[c] PSI Center for Neutron and Muon Sciences, Paul Scherrer Institute, Villigen PSI CH-5232, Switzerland
[d] Kavli Institute of Nanoscience, National Centre for HREM, Delft University of Technology, Lorentzweg 1, Delft 2628 CJ, the Netherlands
[e] Department of Materials Science and Engineering, Faculty of 3mE, Delft University of Technology, Mekelweg 2, Delft 2628 CD, the Netherlands

ARTICLE INFO

Keywords:
Iron alloys
Precipitation kinetics
Deformation
SANS
TEM
Texture

ABSTRACT

In-situ time-resolved small-angle neutron scattering (SANS) experiments were conducted on homogenised cold-rolled ternary Fe-Au-W alloys during aging for 12 h at temperatures of 650 to 700 °C in order to study the kinetics of the nanoscale precipitation. For comparison the precipitation kinetics in the binary counterparts Fe-Au and Fe-W alloys were also studied. In the ternary Fe-Au-W alloy nanoscale Au-rich precipitates were observed by both transmission electron microscopy (TEM) and SANS, while no significant W-rich precipitation was observed. The SANS pattern of the cold-rolled Fe-Au-W alloy clearly reveals a preferred orientation for the plate-shaped nanoscale Au-rich precipitates. As these Au-rich precipitates have a fixed orientation relation with the matrix lattice this preferred orientation originates from the texture of the *bcc* matrix grains, as confirmed by X-ray diffraction (XRD) pole figure measurements. The effect of texture on the nuclear and the magnetic SANS signal during the precipitation kinetics was included in the data analysis. This enables us to monitor the temperature dependence of the precipitation kinetics for the Au-rich precipitates in the Fe-Au-W alloy during aging at temperatures of 650, 675 and 700 °C. It is found that an increase in aging temperature results in a faster kinetics and a lower final precipitate fraction.

1. Introduction

Precipitation plays an important role in designing mechanical properties of advanced structural metals [1–3]. As precipitates act as obstacles to dislocation motion, the hardness, strength and creep resistance can be controlled by the size, distribution and composition of the precipitates. Recently, precipitation has also been used to achieve self healing of creep damage in metal alloys [4–7]. The underlying mechanism for the self healing and the subsequent improvement of the creep lifetime is the site-selective precipitation of supersaturated solute atoms at defect sites, thereby immobilizing further damage growth. Knowledge of the deformation-induced precipitation during aging is therefore of critical importance to fully utilize the precipitation-induced self-healing mechanism in alloys for structural applications.

In order to achieve site-selective precipitation of supersaturated solute exclusively at damage sites, it was found that a sufficiently large atomic size difference between the solute atom and the host atom is required. A large difference in atomic size results in a large strain penalty for homogeneous precipitation in the bulk of the matrix. In previous studies we focussed on Fe-based model alloys with about 1 at.% of added Cu [8], Au [9–12], Mo [13] and W [14]. These alloys all have a *bcc* lattice structure for the matrix of the alloy. The relative atomic size difference $(r_X - r_{Fe})/r_{Fe}$ for the atomic radius of the solute atom (r_X) and the host atom (r_{Fe}) of these elements corresponds to: 0.1 % for Cu, 12.9 % for Au, 9.8 % for Mo and 10.1 % for W. A clear difference in site selectivity for precipitation between Cu and Au was observed [8–10], where Au precipitation was suppressed in the absence of deformation while Cu precipitation was also observed in the undeformed matrix. Self healing of creep damage by site-selective precipitation was established for Fe-Au, Fe-Mo and Fe-W alloys.

* Corresponding author.
E-mail address: n.h.vandijk@tudelft.nl (N.H. van Dijk).

https://doi.org/10.1016/j.mtla.2024.102322
Received 13 December 2024; Accepted 15 December 2024
Available online 16 December 2024

Experimental data on Au-rich precipitation in *bcc* Fe are limited. Early studies [15–18] revealed the presence of plate-shaped precipitates with an *fcc* structure that form with a fixed orientation relation with respect to the *bcc* matrix. As predicted by the Fe-Au phase diagram the Au content of the precipitates depends on the aging temperature. These findings are confirmed in our recent experiments [9–12]. Thermodynamic data for the Fe-Au phase diagram were reported by Liu and co-workers [19]. W-rich precipitation in *bcc* Fe occurs in the form of the hexagonal Fe_2W Laves phase precipitates [14].

To study the interplay between two supersaturated alloying elements in site-selective precipitation the ternary Fe-Au-W alloy was selected (with 1 at.% of supersaturation for both solute elements). For this alloy self healing of creep damage was established, where the formation of Au-rich precipitates was dominant compared to the formation of W-rich precipitates [20,21].

In the present study the effect of mechanical deformation by cold rolling on the precipitation in the ternary Fe-Au-W alloy and its binary Fe-Au and Fe-W counterparts was studied by *in-situ* time-resolved small-angle neutron scattering (SANS) experiments during aging at temperatures between 650 and 700 °C. SANS is a powerful technique that can *in-situ* probe the precipitate size distribution for a relatively large sample volume (several mm^3) [22–28].

First, the effect of the alloy composition is investigated by comparing time-resolved SANS measurements for the Fe-Au-W, Fe-Au and Fe-W alloys at an aging temperature of 650 °C. From these SANS results the precipitation kinetics is investigated in the presence of rolling texture for the matrix grains for the studied alloys. After that, the effect of the aging temperature is investigated for the Fe-Au-W alloy by time-resolved SANS measurements at aging temperatures of 650, 675 and 700 °C.

The cold rolling of the studied samples was introduced to obtain a high density of nucleation sites, which is required for the nucleation of Au-rich and W-rich precipitates. There are no indications that the texture in the Fe-based matrix affects the precipitation kinetics for the Au-rich and W-rich precipitates. Differences in the texture present in the cold-rolled Fe-Au, Fe-W and Fe-Au-W starting materials originates from variations in the production process of the sheet material. As the texture in the cold-rolled starting material affects the data analysis of the precipitate size distribution we have included the preferred orientation in the data analysis of the SANS data to obtain more reliable values for the precipitate size distribution.

2. Experimental

A high purity ternary Fe-Au-W (3.07 wt.% Au and 3.83 wt.% W) alloy, and its binary counterparts Fe-Au (2.87 wt.% Au) and Fe-W (3.80 wt.% W) were produced by Goodfellow in the form of rolled sheet material with a thickness of 0.5 mm. Plate samples with dimensions of about 10×10 mm^2 were cut from the sheet material. To fully dissolve the gold and tungsten atoms, the samples were first held at elevated temperature (868 °C for a period of 5 h for the Fe-Au-W and Fe-Au alloys and 900 °C for a period of 24 h for the Fe-W alloy) in evacuated silica tubes filled with 200 mbar ultra-high-purity argon, followed by a rapid water quench. The composition, annealing condition and final grain size of the alloys is listed in Table S1 (Supplementary Information). To study the effect of deformation damage on the precipitation during aging, the as-quenched samples were cold rolled with a thickness reduction of about 20 %. The total sample thickness and thickness reduction for the studied SANS samples is listed in Table S2 (Supplementary Information).

Time-resolved SANS experiments were performed on the SANS-I instrument at PSI, Switzerland, using a neutron wavelength of $\lambda = 0.7$ nm (with $\Delta\lambda/\lambda = 10$ %) [29]. During these measurements, a stack of 3 high-purity alloy plate samples with a total thickness of about 1.2 mm was mounted in a vacuum furnace ($<10^2$ Pa). The rolling direction of the samples was oriented vertically (and perpendicular to the neutron beam). The time-dependent precipitation was monitored *in situ* during aging for 12 h at a selected constant temperature (650 °C for all three alloys and 650, 675 and 700 °C for the Fe-Au-W alloy). The average heating rate of the SANS furnace was about 100 K/min. The sample-to-detector distance is periodically varied between 2 and 6 m to gain the SANS signals over a wide range of wave vector transfers. An additional sample-to-detector distance of 18 m was used before and after aging to detect the scattering at very small angles. A horizontal magnetic field of 1.2 T was applied to separate the nuclear and magnetic scattering (the field is oriented perpendicular to both the rolling direction and the neutron beam). Further details on the sample composition and dimensions can be found in the supplementary information (Tables S1 and S2). The data reduction of the SANS was done using the BerSANS [30] software and the fitting of the scattering profiles was done using SasView [31].

Transmission electron microscopy (TEM) investigations were carried out on the Fe-Au-W, Fe-Au and Fe-W alloys after the SANS measurements. Disks were mechanically ground down to 20 μm and then thinned to electron transparency by Ar ion milling. The resulting samples were examined using a FEI Cs-corrected cubed Titan instrument, operating at 300 kV, both in TEM mode and scanning mode (STEM). STEM Annular Dark Field (ADF) images were obtained by collecting the scattered electrons on an annular detector for each beam position. Elemental maps were obtained from X-ray spectra collected for each pixel in an ADF image, using the Thermo Fisher Scientific super-X detector in the ChemiSTEM™ configuration. Lattice images were collected on a Thermo Scientific CetaTM 16 M. Microstructures were analysed by scanning electron microscopy (SEM) with a JEOL JSM 6500F scanning electron microscope.

3. Results and discussion

3.1. Transmission electron microscopy

In order to obtain a general characterisation of the precipitates that formed during 12 h aging at 650 °C, the samples were investigated by TEM. In Fig. 1 TEM images of the Au-rich precipitates in the Fe-Au-W alloy after aging are shown. The image in Fig. 1a indicates the presence of a large number of plate-shaped Au-rich precipitates. In between of the precipitates dislocations can be observed, which are expected to originate from the cold rolling and assist in the nucleation of the precipitates. The observed plate-shaped precipitates are all present within the same Fe-based matrix grain with a *bcc* lattice structure. From previous studies [9,11,15,17,18,20] we know that the Au-rich precipitates show a fixed orientation relation with the surrounding matrix phase, where the plate normal is aligned with one of the 3 principle axes of the cubic crystal structure. The orientation relations between the Au-rich precipitate (p) with an *fcc* lattice structure and the matrix (m) with a *bcc* lattice structure correspond to [17]: $(100)_p \| (100)_m$ and $<100>_p \| <110>_m$. This means that three orientations of the plate-shaped precipitates are observed: one orientation where the plate normal is along the viewing direction and two where it is perpendicular. For the first orientation the in-plane dimensions indicate a nearly square shape with rounded corners. The two other orientations give direct information on the plate dimensions. In Fig. S1 (Supplementary Information) the experimental values of the plate length L and the plate thickness δ are shown for the probed precipitates. Based on these observations an effective aspect ratio of $L/\delta = 8.9(5)$ can be deduced for the plate-shaped Au-rich precipitates in the Fe-Au-W alloy after aging (note that the value in between brackets refers to the error in the last digit). The size distribution of the precipitate reflects the time of nucleation where large precipitates are expected to correspond to an early time of nucleation. Within the accuracy no size dependence for the aspect ratio is found. A size dependent aspect ratio would be signalled by a deviation from a linear trend through the origin. Literature data on this topic are limited. Aaronson and coworkers [44] have shown that grain-boundary precipitates in Fe-C binary alloys show a precipitate growth with a fixed aspect ratio as a function of time, temperature and

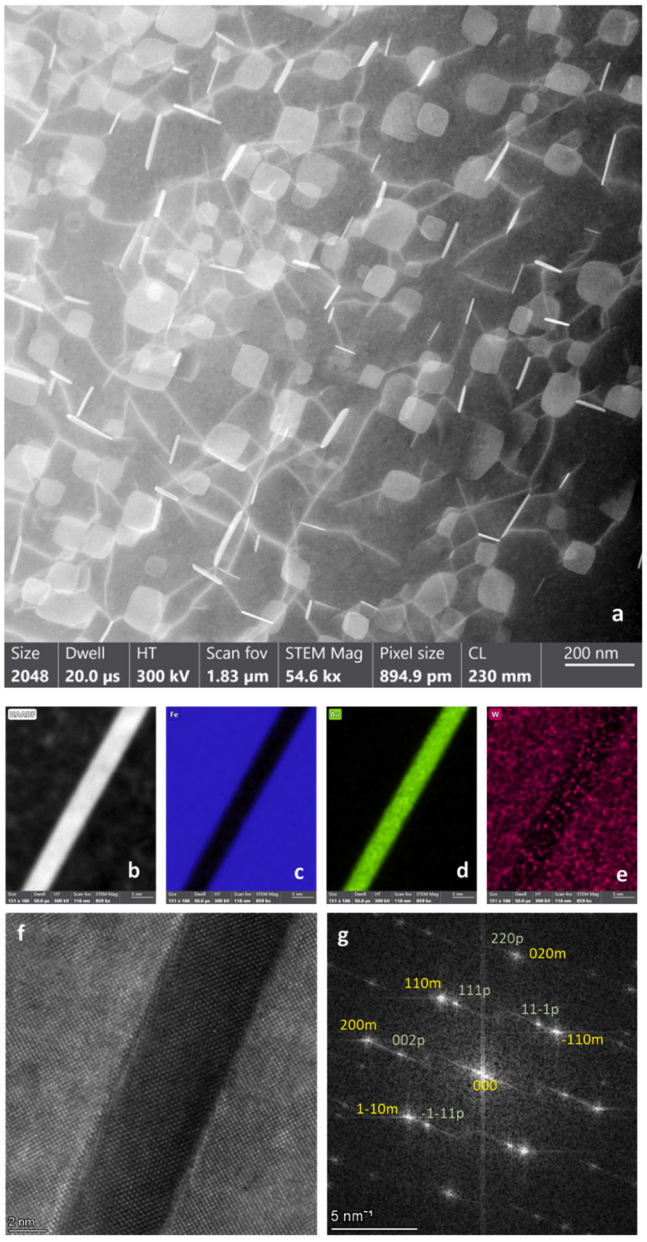

Fig. 1. STEM and TEM images of the cold-rolled homogenised Fe-Au-W alloy after 12 h of aging at a temperature of 650 °C. Au-rich plate-shaped precipitates are clearly visible in (a). The Au-rich precipitate in (b) was analysed to map the (c) Fe, (d) Au and (e) W concentration. The precipitate contains about 60 at.% Au and no indication for the presence of W was found. (f) High resolution image of the precipitate and the surrounding matrix. (g) FFT image of (f) indicating the following orientation relations between the *bcc* matrix (*m*) and the *fcc* precipitate (*p*): $[001]_m \parallel [1\text{–}10]_p$ and $[020]_m \parallel [220]_p$ in agreement with the previously reported orientation relation [15,17].

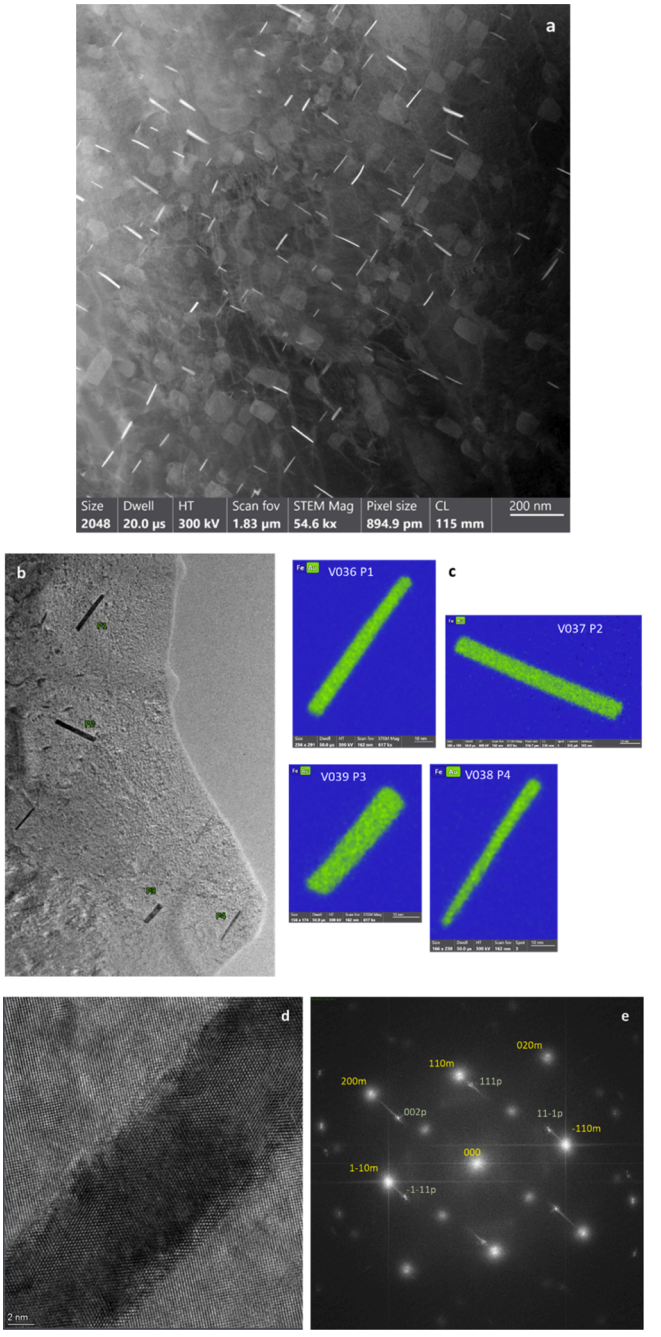

Fig. 2. STEM and TEM images of the cold-rolled homogenised Fe-Au alloy after 12 h of aging at a temperature of 650 °C. Au-rich plate-shaped precipitates are clearly visible in (a). The Au-rich precipitate in (b) was analysed to map the (c) Au concentration. The precipitate contains about 60 at.% Au. (d) High resolution image of the precipitate and the surrounding matrix. (e) FFT image of (d) confirming the previously reported orientation relation between the *bcc* matrix and the *fcc* precipitate for Fe-Au alloys [15,17].

carbon content. The present case Au-rich precipitates nucleate and grow on dislocations (sub-grain boundaries), which may be regarded as a related case.

In Fig. 2 TEM images for the Fe-Au alloys after aging at 650 °C are shown, confirming the presence of plate-shaped Au-rich precipitates in the Fe-Au alloy. In the Fe-Au alloy after aging the plate-shaped Au-rich precipitates were found to show an effective aspect ratio of $L/\delta = 8.2(3)$. This value is found to be in agreement with the value of $L/\delta \approx 8$ obtained in previous results for a tensile deformed Fe-Au alloy during aging at 550 °C [9].

As indicated in Fig. 1b–e the Au-rich precipitates in the Fe-Au-W alloy contain about 60 at.% Au with balance Fe (about 40 at.% Fe) and a minor W content (below the matrix concentration of 1.2 at.% W). The Au concentration of the Au-rich precipitate is in agreement with the results for the Fe-Au alloy in Fig. 2c. As indicated from the results in Fig. 1f, g, the Au-rich *fcc* plate-shaped precipitates (p) show a fixed orientation relation with the *bcc* matrix (m) in Fe-Au-W alloy (see Fig. 2d-2e for the Fe-Au alloy), in agreement with the previously reported $[010]_p \parallel [110]_m$ orientation relation [15,17]. In Fig. 3 TEM images for Fe-W alloy after aging at 650 °C are shown. The Fe-W alloy does not show W-rich precipitation after 12 h of aging at 650 °C. The

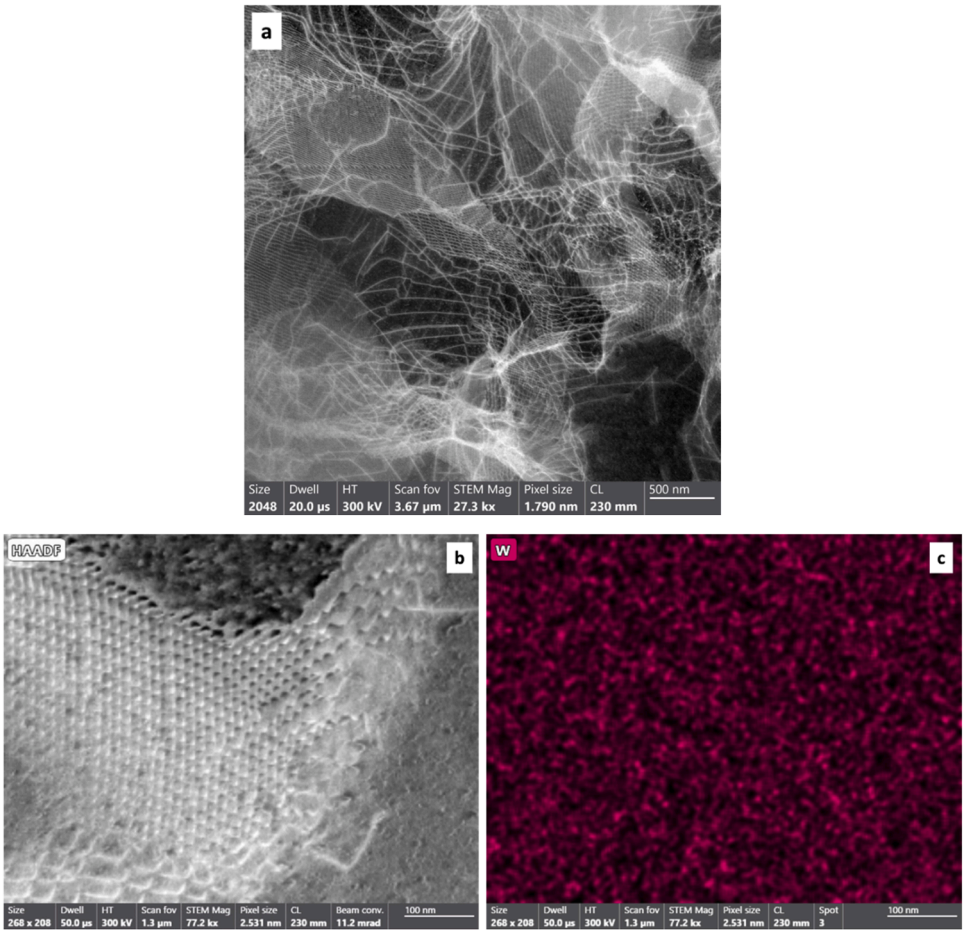

Fig. 3. STEM images of the cold-rolled homogenised Fe-W alloy after 12 h of aging at a temperature of 650 °C. Dislocation networks are clearly visible in (a). The area of the dislocation network in (b) was also analysed to map the W concentration (c). No indication for the formation of W-rich precipitates was found.

aged cold-rolled Fe-W alloy shows a pronounced nanoscale dislocation network, indicating the formation of sub-grains.

3.2. *Small-angle neutron scattering*

Fig. 4 shows the experimental 2D SANS patterns of the homogenised and cold-rolled Fe-Au-W, Fe-Au and Fe-W alloys before (top row) and after (bottom row) 12 h of aging at a temperature of 650 °C. All patterns were collected at room temperature in a horizontal applied magnetic field of 1.2 T to magnetically saturate the ferromagnetic matrix phase. It can be seen that: (1) for the gold-containing Fe-Au-W and Fe-Au alloys the SANS intensity has largely increased as a result of Au-rich precipitation during the aging. (2) For the Fe-W alloy, however, no significant increase in SANS signal was observed, indicating that this aging step did not generate a significant amount of W-rich precipitation. (3) Both the Fe-Au-W and Fe-Au alloys show a strongly anisotropic SANS pattern with the strongest scattering oriented perpendicular to the applied field. This indicates a strong magnetic SANS contribution. (4) The angular dependence of the SANS signal of the Fe-Au-W alloy is rather different from that of the Fe-Au alloy. The angular dependence of the SANS pattern of the Fe-Au alloy resembles that of our previous SANS measurements on Fe-Au [9] alloys with tensile deformation, reflecting a SANS pattern originating from randomly oriented plate-shaped precipitates (Fe-Au) embedded in a magnetically aligned ferromagnetic matrix (randomly in the scattering plane probed in the SANS experiment). This suggests that the Fe-Au-W alloy shows a significant preferred orientation for the Au-rich plate precipitates. This preferred orientation of the Au-rich plate precipitates is expected to originate from texture in the matrix grains induced by the cold rolling. The relative strength of the magnetic and the nuclear SANS for the Au-rich precipitates in the ferromagnetic matrix is estimated in Fig. S2 of the Supplementary information. The SANS patterns at different distances for the Fe-Au-W (Fig. S3), Fe-Au (Fig. S4) and Fe-W (Fig. S5) alloys can be found in the Supplementary Information.

The SANS intensity from a distribution of precipitates embedded in a magnetically aligned ferromagnetic matrix can be expressed as the sum of the nuclear and the magnetic scattering [24]:

$$\left(\frac{d\Sigma}{d\Omega}\right)_{tot}(\mathbf{Q}) = \left(\frac{d\Sigma}{d\Omega}\right)_{N}(\mathbf{Q}) + \sin^2(\alpha)\left(\frac{d\Sigma}{d\Omega}\right)_{M}(\mathbf{Q}) \quad (1)$$

where the indices N and M refer to the nuclear scattering and the magnetic scattering, respectively. The scattered intensity is represented as $(d\Sigma/d\Omega)(\mathbf{Q})$, which refers to the differential of the macroscopic scattering cross section Σ to the solid angle Ω at a given wave vector transfer $\mathbf{Q}$. In a small angle scattering experiment the wave vector transfer $\mathbf{Q}$ is oriented perpendicular to the neutron beam (x axis). It can be expressed as $\mathbf{Q} = Q\ (0, \cos(\alpha), \sin(\alpha))$, where α is the angle with respect to the applied magnetic field ($\alpha = 0$) and $Q = |\mathbf{Q}| = (4\pi/\lambda)\sin(\theta)$ is the amplitude of the wave vector transfer for a scattering angle 2θ and a neutron wave length λ. Compared to the nuclear scattering from precipitates, the magnetic scattering has an additional angular dependent $\sin^2(\alpha)$ term. The $\sin^2(\alpha)$ originates from the nature of the magnetic scattering which only gives a contribution when the spin component that is perpendicular to the scattering vector $\mathbf{Q}$.

For paramagnetic precipitates with fixed relative dimensions embedded in a magnetically aligned ferromagnetic matrix the nuclear

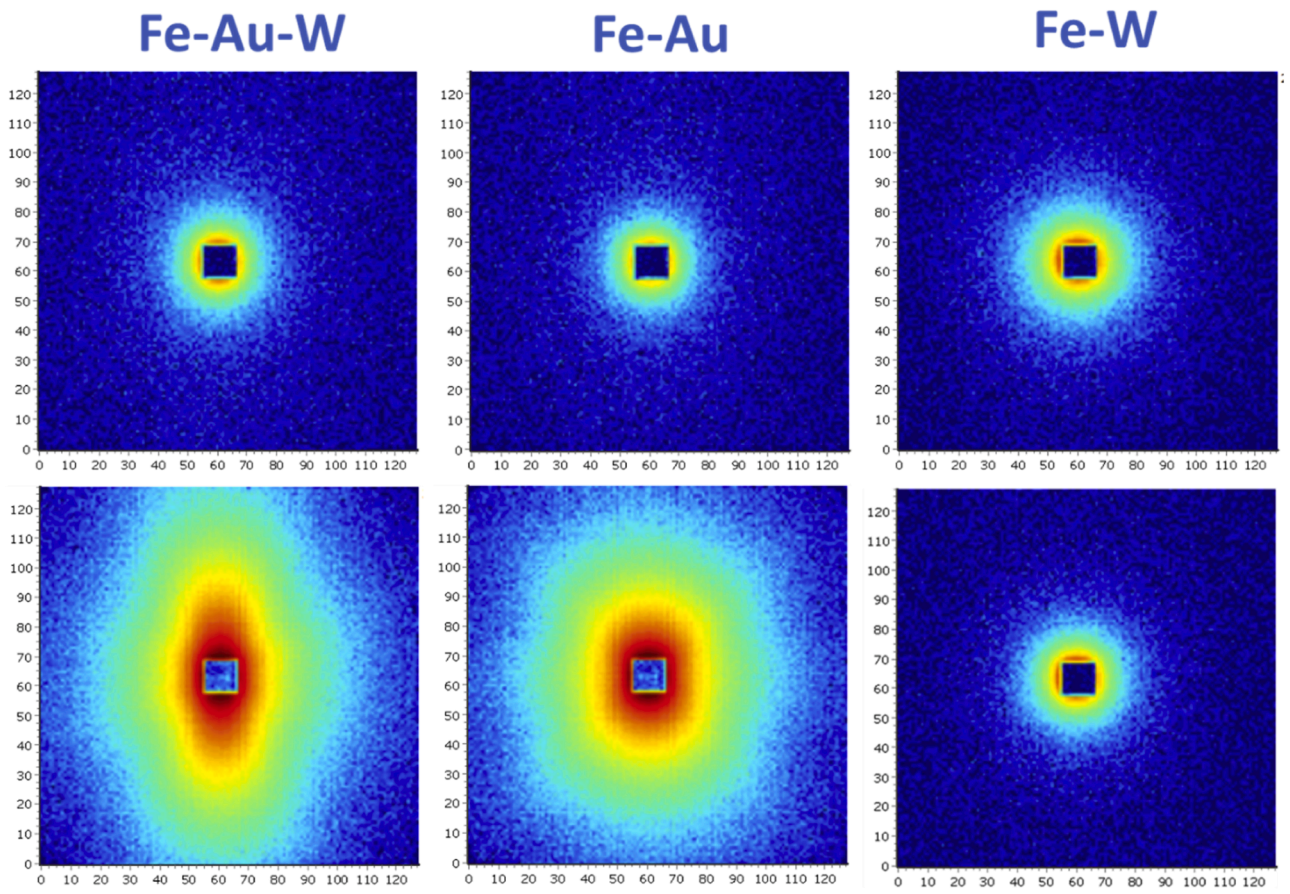

Fig. 4. SANS intensity (log scale) patterns on the 2D detector for the Fe-Au-W, Fe-Au and Fe-W alloys before (top row) and after (bottom row) 12 h aging at a temperature of 650 °C. The samples were cold rolled with a thickness reduction of about 20 % prior to the SANS experiments. The difference originates from the formation of nanoscale precipitates. The SANS measurements were performed at room temperature using a neutron wave length of $\lambda = 0.7$ nm and a sample-to-detector distance of $L_{sd} = 6$ m. The ferromagnetic Fe-based matrix is magnetically saturated in a horizontal magnetic field (1.2 T). The intensity is plotted on a logarithmic scale.

and magnetic SANS can be represented as:

$$\left(\frac{d\Sigma}{d\Omega}\right)_N(\mathbf{Q}) = (\Delta\rho_N)^2 \int_0^\infty D_N(\delta)V^2(\delta)P(\mathbf{Q})d\delta + \left(\frac{d\Sigma}{d\Omega}\right)_{bg} \quad (2)$$

$$\left(\frac{d\Sigma}{d\Omega}\right)_M(\mathbf{Q}) = (\Delta\rho_M)^2 \int_0^\infty D_N(\delta)V^2(\delta)P(\mathbf{Q})d\delta \quad (3)$$

where $\Delta\rho_N$ and $\Delta\rho_M$ are respectively the difference in nuclear and the difference in magnetic scattering length density between the precipitate and the matrix. Details on their mathematical evaluation can be found in the Supplementary Information (Table S3). For the strength of the magnetic moment of the Fe atoms in the *bcc* matrix phase the data from Arrott and Heinrich [32] are used. The relative strength of the magnetic and nuclear scattering from a precipitate is given by the contrast ratio $A = (\Delta\rho_M)^2/(\Delta\rho_N)^2$. As indicated in Table S3 the magnetic scattering is expected to be dominant, both at room temperature and at elevated temperatures (650 °C). The nuclear scattering contains an additional background term, which originates from the incoherent neutron scattering and the temperature-dependent thermal diffuse scattering. Based on the TEM data in Fig. 2 the precipitates are assumed to be rectangular plates with a thickness δ, two equal long axes with length L and a volume $V(\delta) = L^2\delta$. The aspect ratio $\eta = L/\delta$ is fixed to the experimental value obtained by TEM. The number distribution $D_N(\delta)$ for the precipitates is assumed to correspond to a lognormal distribution:

$$D_N(\delta) = \frac{N_p}{\delta\sigma\sqrt{2\pi}}\exp\left(-\frac{[\ln(\delta) - \ln(\delta_m)]^2}{2\sigma^2}\right) \quad (4)$$

Integration over all sizes provides the number density of precipitates N_p. The number distribution is related to the volume size distribution by $D_V(\delta) = D_N(\delta)V(\delta)$. Integration of the volume distribution over all sizes provides the phase fraction of precipitates f_p (with a maximum value of about 1 % for the present alloys). The scattering factor of the precipitates $P(\mathbf{Q}) = \left\langle |F(\mathbf{Q})|^2 \right\rangle$ is defined by the orientation dependent form factor $F(\mathbf{Q})$ [33,34] with:

$$|F(\mathbf{Q})|^2 = \left|\frac{\sin(u)}{u}\right|^2 \left|\frac{\sin(v)}{v}\right|^2 \left|\frac{\sin(w)}{w}\right|^2 \quad (5)$$

where $u = \frac{1}{2}L(\hat{\mathbf{a}}\cdot\mathbf{Q})$, $v = \frac{1}{2}L(\hat{\mathbf{b}}\cdot\mathbf{Q})$ and $w = \frac{1}{2}\delta(\hat{\mathbf{c}}\cdot\mathbf{Q})$. Unit vectors $\hat{\mathbf{a}}$, $\hat{\mathbf{b}}$ and $\hat{\mathbf{c}}$ are the principle axis directions of the precipitate. $\hat{\mathbf{a}}$ and $\hat{\mathbf{b}}$ are in the plane of the plate-shaped precipitate (length L) and $\hat{\mathbf{c}}$ normal to the plane of the plate-shaped precipitate (length δ).

For an orientation distribution of the plate normal of the plate-shaped precipitates can in general be described with an orientation function $p(\theta, \varphi, \psi)$ with polar angles θ and φ of the plate normal of the precipitate with respect to the beam direction and angle ψ characterising the plate orientation with respect to the plate normal. The orientation function $p(\theta, \varphi, \psi)$ is normalised as $\frac{1}{8\pi^2}\int_0^\pi\int_0^{2\pi}\int_0^{2\pi} p(\theta, \varphi,$

$\psi)|F(\mathbf{Q})|^2\sin(\theta)d\theta d\varphi d\psi = 1$, with $p(\theta,\varphi,\psi) = 1$ for a random orientation. The scattering factor $P(\mathbf{Q})$ is defined as:

$$P(\mathbf{Q}) = \left\langle |F(\mathbf{Q})|^2 \right\rangle = \frac{1}{8\pi^2}\int_0^{\pi}\int_0^{2\pi}\int_0^{2\pi} p(\theta,\varphi,\psi)|F(\mathbf{Q})|^2\sin(\theta)d\theta d\varphi d\psi \quad (6)$$

For thin plates ($\eta = L/\delta \gg 1$) the form factor can be approximated for $Q \gg 1/L$ by:

$$|F(\mathbf{Q})|^2 \approx \left(\frac{2\pi}{LQ}\right)^2 \left|\frac{\sin(\delta Q/2)}{\delta Q/2}\right|^2 [\delta(\hat{\mathbf{Q}} - \hat{\mathbf{c}}) + \delta(\hat{\mathbf{Q}} + \hat{\mathbf{c}})] \quad (7)$$

This indicates that for thin plates with $\eta = L/\delta \gg 1$ constructive interference only takes place when the scattering vector $\mathbf{Q}$ is aligned along one of the plane normal vectors of the plate oriented along $+\hat{\mathbf{c}}$ and $-\hat{\mathbf{c}}$. In a SANS experiment only the $\mathbf{Q} = Q(0, \cos(\alpha), \sin(\alpha))$ vectors perpendicular to the beam are probed. The orientation averaged scattering factor corresponds to:

$$P(\mathbf{Q}) \approx f(\alpha)\left(\frac{2\pi}{LQ}\right)^2 \left|\frac{\sin(\delta Q/2)}{\delta Q/2}\right|^2 \quad (8)$$

For $1/L \ll Q \ll 1/\delta$ the SANS signal follows the well-known Q^{-2} dependence for thin flat particles, while it follows the Porod law with Q^{-4} for $Q \gg 1/\delta$. The factor $f(\alpha)$ describes the relative orientational weight for precipitate plate normal in the SANS scattering plane (perpendicular to the neutron beam), and thereby defines the anisotropy of the nuclear SANS on the 2D detector. In our present cold-rolled samples a symmetry of the type $f(\alpha) = f(-\alpha) = f(\pi - \alpha)$ is expected. This can be modelled by [35]:

$$f(\alpha) = 1 + C_2\cos(2\alpha) + C_4\cos(4\alpha) \quad (9)$$

Angular averaging gives $< f > = 1$ and characteristic values are: $f(0) = 1 + C_2 + C_4$, $f(\pi/4) = 1 - C_4$ and $f(\pi/2) = 1 - C_2 + C_4$. An isotropic angular distribution without texture corresponds to $f(\alpha) = 1$ with $C_2 = C_4 = 0$. Higher order terms, like $C_6\cos(6\alpha)$, were not found to significantly contribute and were therefore ignored.

In Fig. 5 the Q dependence of the SANS pattern of the Fe-Au-W alloy before and after 12 h of aging at 650 °C is shown for the nuclear scattering $(d\Sigma/d\Omega)_N(\mathbf{Q})$ along the magnetic field ($\alpha = 0°$) and the magnetic scattering $(d\Sigma/d\Omega)_M(\mathbf{Q})$ perpendicular to the field ($\alpha = 90°$). Along the field the magnetic scattering is absent, and as a result all scattering corresponds to nuclear SANS from the precipitates and background scattering. Perpendicular to the field the total scattering corresponds to magnetic and nuclear scattering from the precipitates and background. By scaling the background corrected total SANS signal $(d\Sigma/d\Omega)^{cor}_{tot}(\mathbf{Q})$ with a factor $A/(A+1)$, the magnetic SANS is obtained. Both the nuclear and the magnetic SANS show a significant increase as a result of the formation of Au-rich precipitates. The largest signal is obtained from the magnetic SANS, which is in line with the relatively large contrast ratio ($A \approx 4$ at room temperature). The corresponding figures for the Fe-Au alloy is shown in Fig. 6 and for the Fe-W alloy in Fig. 7. A direct comparison of the nuclear and magnetic SANS contributions of the plate-shaped Au-rich precipitates at a given angle α requires texture information for the preferred orientation of the precipitates. As can be seen in Figs. 5–7 the SANS patterns before aging contain a Q^{-4} power law contribution originating from grain boundary scattering for both nuclear and magnetic scattering. In addition, the nuclear scattering contains a constant background that originates from incoherent scattering. This incoherent scattering background is not present in magnetic SANS. The additional scattering for finite aging times now originates from the precipitation scattering and has the same form for both the nuclear and the magnetic scattering, but with a different contrast.

In Fig. 8 the angular dependence of the SANS pattern of the Fe-Au-W alloy after 12 h of aging at 650 °C is shown for the nuclear scattering $(d\Sigma/d\Omega)_N(\mathbf{Q})$ and the magnetic scattering $\sin^2(\alpha)(d\Sigma/d\Omega)_M(\mathbf{Q})$ from the precipitates at different Q values. From the background corrected total SANS signal $(d\Sigma/d\Omega)^{cor}_{tot}(\mathbf{Q})$ the nuclear SANS from the precipitates $(d\Sigma/d\Omega)_N(\mathbf{Q})$ is obtained by scaling with a factor $1/(A\sin^2(\alpha)+1)$ and the magnetic SANS from the precipitates $\sin^2(\alpha)(d\Sigma/d\Omega)_M(\mathbf{Q})$ is obtained by scaling with a factor $A\sin^2(\alpha)/(A\sin^2(\alpha)+1)$. The angular dependence of the nuclear scattering reveals a significant texture with a minimum value for $\alpha \approx 45°$, which can accurately be fitted using the angular distribution function of Eq. (6) with texture parameters $C_2 = -0.19$ and $C_4 = 0.37$. For the magnetic scattering $\sin^2(\alpha)$ term suppresses the signal along the applied magnetic field ($\alpha = 0°$). The standard deviation of the texture function $f(\alpha)$ corresponds to: $\sigma_f = \left[< f^2 > - < f >^2\right]^{1/2} = \left[(C_2)^2/2 + (C_4)^2/2\right]^{1/2} = 0.29$. The texture in the Fe-Au alloy is significantly weaker (see Fig. S6 in Supplementary Information) with $C_2 = 0.20$ and $C_4 = 0.05$. The fitted texture parameters at elevated temperatures are listed in Table S4 (Supplementary Information).

As the magnetic SANS is dominant, this contribution is used to study the precipitation kinetics of the Au-rich precipitates. The SANS curves for different aging times were fitted with the SASview data analysis software [31]. Using the described model assumptions the lognormal precipitate size distribution was obtained for plate-shaped samples with a fixed aspect ratio. Integrating the size distribution obtained by the model fit then gives the precipitate phase fraction f_p.

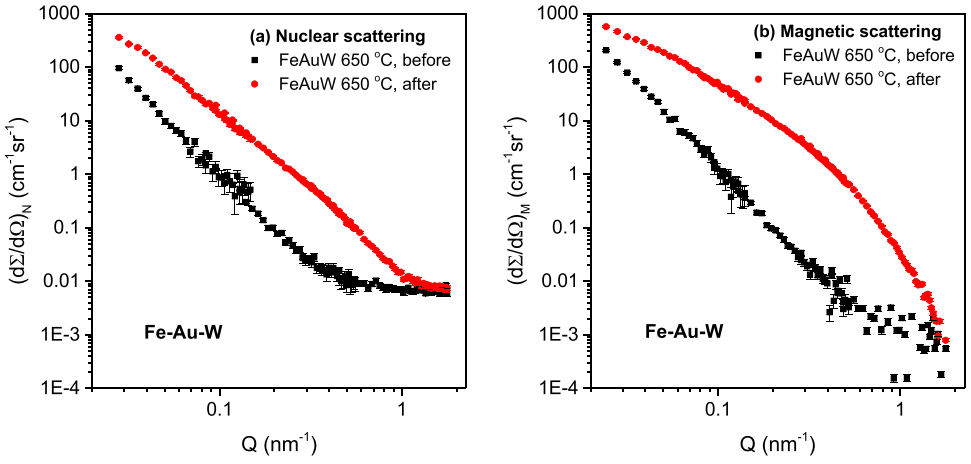

Fig. 5. SANS profiles for the Fe-Au-W alloy measured at room temperature before and after 12 h of aging at 650 °C showing: (a) nuclear scattering $(d\Sigma/d\Omega)_N(Q)$ for $\alpha = 0°$, (b) magnetic scattering $(d\Sigma/d\Omega)_M(Q)$ for $\alpha = 90°$.

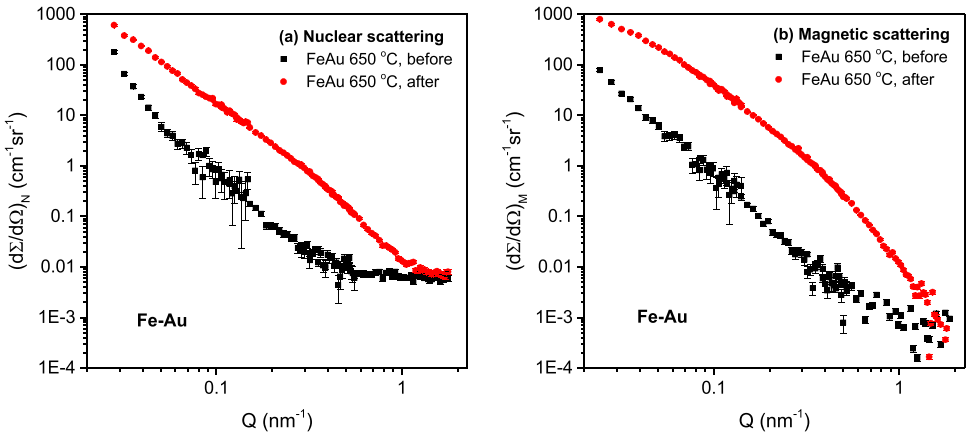

Fig. 6. *Q*-dependent SANS for the Fe-Au alloy before and after aging for 12 h at 650 °C for (a) nuclear scattering $(d\Sigma/d\Omega)_N(Q)$ for $\alpha = 0°$, (b) magnetic scattering $(d\Sigma/d\Omega)_M(Q)$ for $\alpha = 90°$.

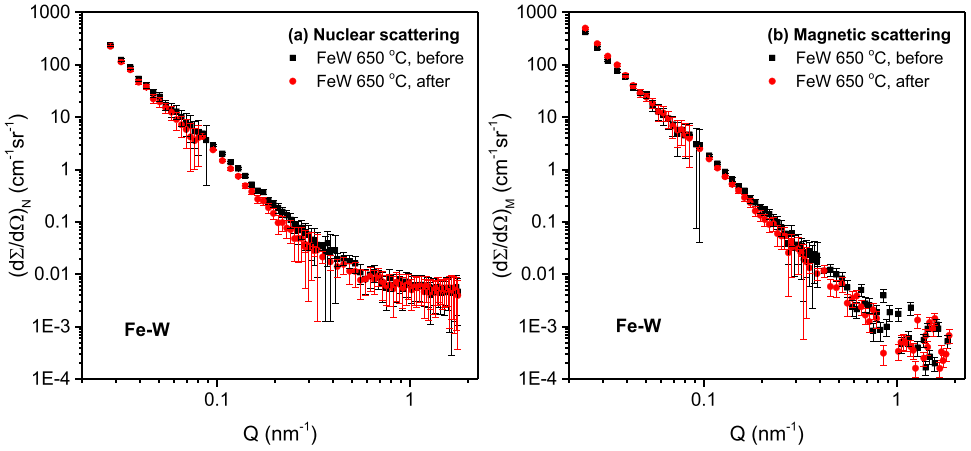

Fig. 7. *Q*-dependent SANS for the Fe-W alloy before and after aging for 12 h at 650 °C for (a) nuclear scattering $(d\Sigma/d\Omega)_N(Q)$ for $\alpha = 0°$, (b) magnetic scattering $(d\Sigma/d\Omega)_M(Q)$ for $\alpha = 90°$.

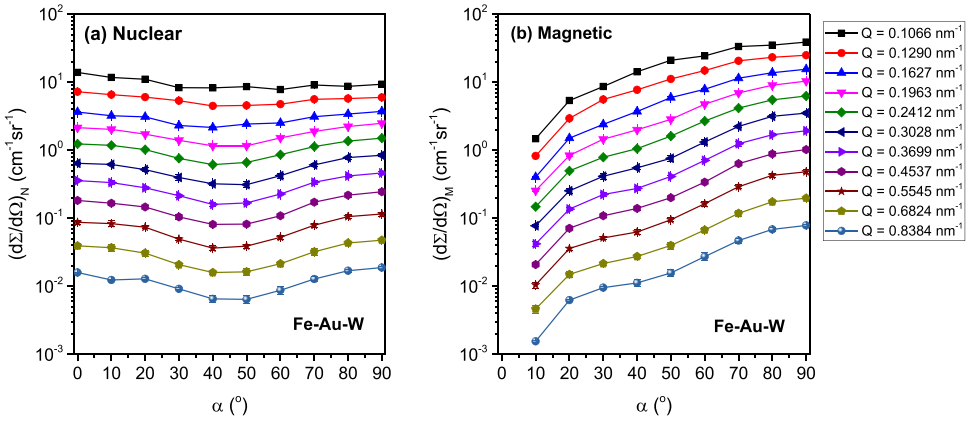

Fig. 8. Angular SANS profiles for the Fe-Au-W alloy measured at room temperature after 12 h of aging at 650 °C showing the scattered intensity $(d\Sigma/d\Omega)(Q)$ as a function of the azimuth angle α with respect to the applied field at $\alpha = 0°$. The SANS patterns are shown for different values for the wave vector transfer *Q*. The panels indicate: (a) nuclear scattering $(d\Sigma/d\Omega)_N(Q)$ and (b) magnetic scattering $\sin^2(\alpha)(d\Sigma/d\Omega)_M(Q)$.

3.3. X-ray diffraction pole figures

The difference in texture parameters for the Fe-Au-W and Fe-Au alloys, as obtained from the angular-dependent SANS, has independently been evaluated by additional XRD pole figure measurements. The (200) XRD pole figures of the *bcc* matrix grains in the Fe-Au-W and Fe-Au alloys are presented in Fig. S7 (Supplementary Information). The (200) pole figures of both alloys do show a texture that is indeed distinctly different for both alloys. As the plate normal of the Au-rich precipitates is aligned with the (200) orientation of the *bcc* matrix grains and because SANS probes the scattering with **Q** perpendicular to the neutron beam, the texture components of interest correspond to the circular edge ($\psi =$

90°) in the (200) XRD pole figure of the *bcc* matrix grains. The C_2 and C_4 texture parameters obtained from SANS are in qualitative agreement with the experimental (200) XRD pole figures for the *bcc* matrix grains.

3.4. Precipitation kinetics of Au-rich precipitates

In Fig. 9 the precipitation kinetics of the Au-rich plate-shaped precipitates is shown for the ternary Fe-Au-W alloy and the binary Fe-Au alloy during aging at a constant temperature of 650 °C. The Au-rich precipitate phase fraction f_p of both alloys shows a very similar time evolution. Around an aging time of 6 h the phase fraction starts to saturate at a fraction of about 0.4 %. These results indicate that the presence of W in the ternary Fe-Au-W alloy has a negligible effect on the nucleation and growth of the Au-rich precipitates. Note that the Au-rich precipitation can start when supersaturation is reached, which is at a lower temperature than the selected aging temperatures.

For the ternary Fe-Au-W alloy the temperature dependence of the Au-rich precipitation kinetics is studied in more detail. In Fig. 10 the time evolution for the (volume) size distribution of the plate-shaped Au-rich precipitates is presented for aging temperatures of 650, 675 and 700 °C. For all aging temperatures the position of the maximum in the distribution increases continuously with time, indicating a continuous plate thickening, and correspondingly, a continuous growth of the plate volume (again L/δ is assumed constant in the analysis). The maximum value in the distribution itself first increases and in the later stage decreases again. The decrease in the maximum value reflects an increase in the width of the distribution once the precipitate phase fraction starts to saturate.

In Fig. 11 the precipitate fraction and the precipitate plate thickness are shown as a function of the aging time for the three studied aging temperatures of 650, 675 and 700 °C. These curves were directly obtained from the time evolution of the (volume) size distribution for the plate-shaped precipitates. Comparing the precipitate fraction for different aging temperatures we find that (*i*) the kinetics goes faster for higher temperatures and (*ii*) the final saturation precipitate fraction slightly decreases at higher temperatures. For increasing temperatures an acceleration of the precipitation kinetics is expected as the solute diffusivity of Au in *bcc* Fe is enhanced for higher temperatures [36]. For higher aging temperatures a reduction in the final precipitate fraction is also expected as the Au solubility in the *bcc* matrix increases with temperature, and as a result, the equilibrium precipitate fraction decreases with temperature. For the kinetics of the precipitate thickness similar trends as the precipitate fraction are observed (with lower statistics).

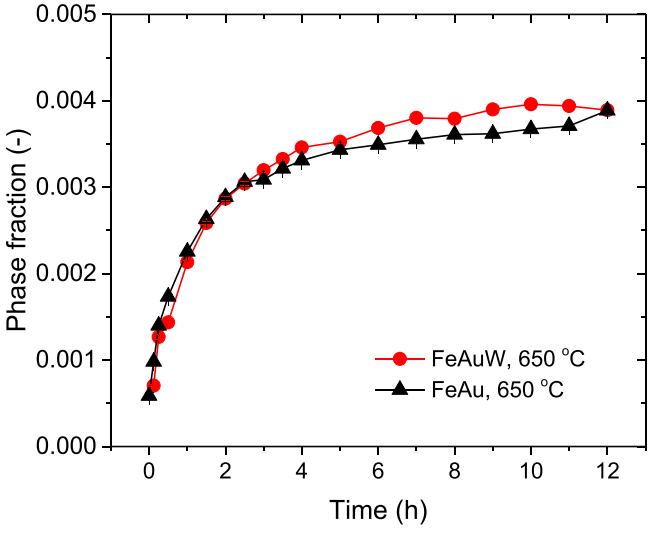

Fig. 9. Precipitate phase fraction f_p of Au-rich plate-shaped precipitates in the Fe-Au-W and Fe-Au alloys for different aging times at 650 °C.

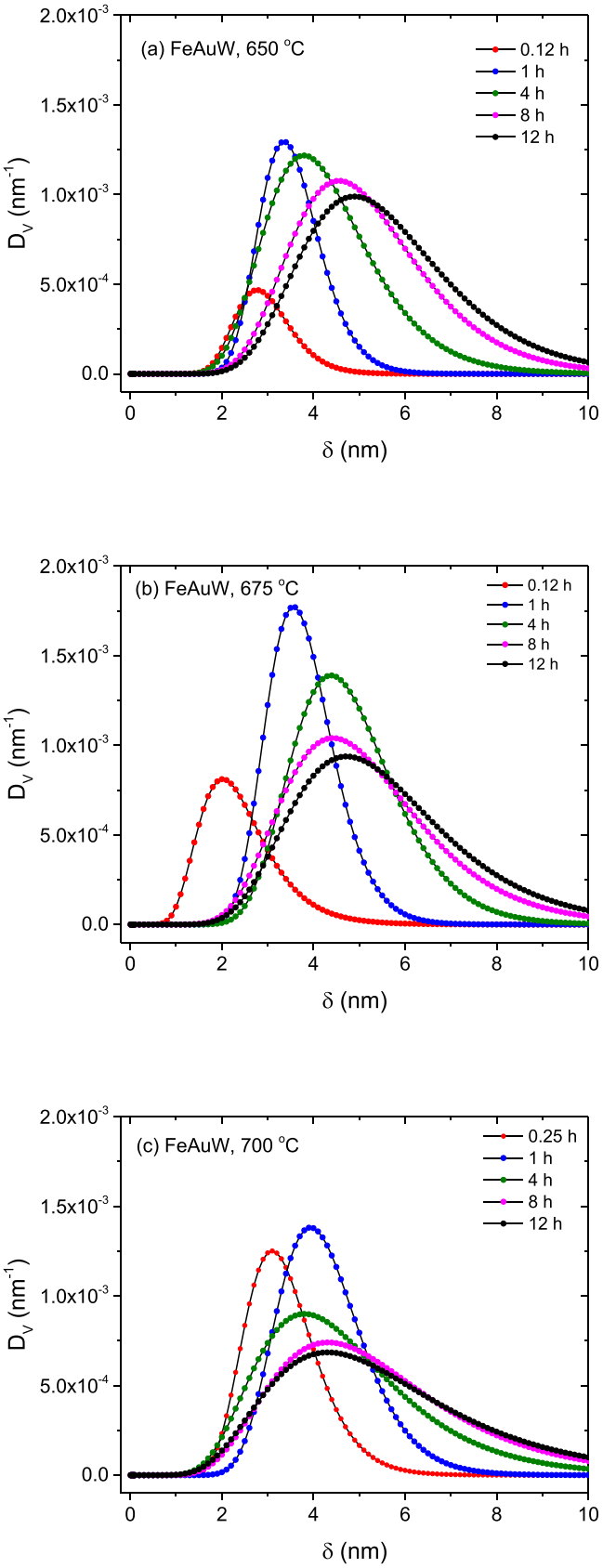

Fig. 10. Volume size distribution $D_V(\delta)$ for the Au-rich plate-shaped precipitates in the Fe-Au-W alloy at different aging times for an aging temperature of (a) 650 °C, (b) 675 °C and (c) 700 °C. The volume size distribution is related to the number size distribution by $D_V(\delta) = V(\delta)D_N(\delta)$, where $V(\delta)$ is the volume of the precipitate.

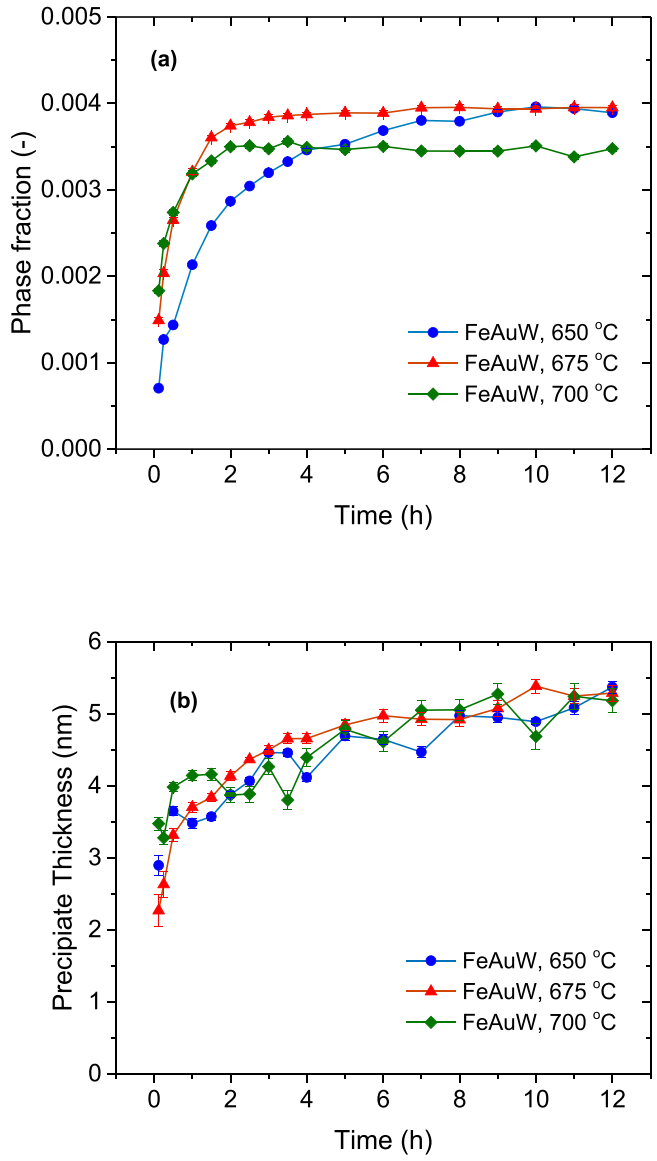

Fig. 11. (a) Precipitate phase fraction f_p and (b) precipitate plate thickness δ of the Au-rich plate-shaped precipitates in the Fe-Au-W alloy as a function of the aging time for aging temperatures of 650, 675 and 700 °C.

The average inter-precipitate spacing Δ can be estimated from the precipitate phase fraction and the precipitate volume by assuming a cubic box with side Δ around each precipitate. A mass balance then leads to: $\Delta^3 f_p = \delta L^2 = \delta^3 (L/\delta)^2$, resulting in $\Delta = (L/\delta)^{2/3} f_p^{-1/3} \delta$. For the Fe-Au-W alloy after 12 h of aging at 650 °C the average inter-precipitate spacing is estimated from the data in Fig. 11 at Δ ≈ 135 nm. This is in qualitative agreement with the TEM data.

To quantitatively analyse the precipitation kinetics we fitted the precipitate fraction as a function of aging time with the Johnson-Mehl-Avrami-Kolmogorov (JMAK) model [37–41]:

$$f_p(t) = f_0[1 - \exp(-kt^n)] \tag{10}$$

Independent fits at variable temperatures resulted in an Avrami constant of $n = 0.73(2)$, 0.78(2) and 0.71(3) for an aging temperature of 650, 675 and 700 °C, respectively (see Fig. S8 and Table S5 in Supplementary Information). In order to evaluate the temperature dependence of the rate constant k, the Avrami constant n was fixed at its value at 650 °C ($n = 0.73$). Fits of the transformation kinetics at fixed n are presented in Fig. S9 and Table S6 (Supplementary Information).

Traditionally the JMAK model predicts an Avrami constant in the range of $n = 1$ - 4, depending on the type of nucleation (steady-state nucleation or instantaneous nucleation) and the dimensionality d of the particle growth (assuming a linear growth rate). However, as discussed by Laplanche [42,43] systems that show a transformation kinetics with an Avrami constant slightly below $n = 1$ are experimentally not uncommon in precipitation kinetics. Precipitation systems with instantaneously forming nuclei located at (sub-)grain boundaries often show a precipitate growth with a reduced growth exponent (slower than linear growth) [44]. The SANS signal in the quenched homogenized samples confirms that no precipitates were formed before the heating to the aging temperature was initiated. The low Avrami constant n experimentally probed for the transformation kinetics in our SANS experiments indicates that the nucleation process occurs effectively instantaneously at the start of the precipitation kinetics. In the present system a relatively high nucleation density with a short average precipitate spacing estimated at Δ ≈ 135 nm was found. The high nucleation density is expected to originate from the high dislocation density associated with the sub-grain microstructure observed in the TEM studies. The sub-grain size was found to be of the same order as the average precipitate spacing. As on the one hand the equilibrium solubility of Au is low in the *bcc* matrix phase and on the other hand the precipitate is rich in Au, the length of the solute diffusion profile in front of the advancing precipitate-matrix interface is in generally much larger than the size of the precipitate (in this case about a factor 100). As a result, soft impingement of overlapping diffusion fields already occurs in the very early stages of the transformation (after the precipitate plate thickness is larger than about 1 nm).

For a diffusional phase transformation the temperature dependence of the rate constant k can be described by an Arrhenius type equation [42]:

$$k = k_0 \exp\left(-\frac{Q_0}{RT}\right) \tag{11}$$

where k_0 is a constant, Q_0 is the activation energy for atom diffusion (of solute atom X) and R is the gas constant. A fit of the temperature dependence of k results in and activation energy $Q_0 = 186(29)$ kJ/mol (Fig. S10 in Supplementary Information). This value is in agreement with the reported activation energy of $Q_0 = 229$ kJ/mol for the atom diffusion of solute Au in a *bcc* Fe matrix [36].

These observations indicate that the precipitation kinetics corresponds to the growth of nuclei that were instantaneously formed at the start of the aging period. These precipitates are located at the cellular dislocation network of the sub-grains, which was formed by the cold rolling step. The overall transformation kinetics was described by a relatively low Avrami constant of $n = 0.73$. As the ratio of the precipitate plate length and its thickness (L/δ) is about constant the precipitate thickness is expected to show a reduced exponential growth with $\delta \propto t^{n/3}$. As a result of the high density of nuclei soft impingement with overlapping diffusion fields in the matrix takes place during most of the diffusion-controlled transformation kinetics.

It is interesting to note that Zhang and co-workers [45] previously reported the presence of solute-rich embryos in a Cu containing multi-component ferritic steel with a nominal composition of Fe-1.5Mn-2.5Cu-4.0Ni-1.0Al (wt.%). These embryos, with a fixed radius of 0.4 nm, were obtained in combination with the nucleation and growth of larger Cu-rich precipitates from a bimodal size distribution in the SANS signal during aging at a temperature of 500 °C and were proposed to act as effective nucleation sites for Cu-rich precipitation. Our present nuclear and magnetic SANS data for binary Fe-Au and ternary Fe-Au-W alloys do not show a bimodal precipitate size distribution for any of the studied aging temperatures (650 to 700 °C) and aging times. This is confirmed by our previous SANS experiments on binary Fe-Cu [8] and binary Fe-Au [9] alloys (for an aging temperature of 550 °C). This absence of a bimodal precipitate distribution indicates that the

solute-rich embryos reported by Zhang and coworkers [45] were not observed in our alloys.

The present precipitation kinetics of Au-rich and W-rich precipitates can be compared with the previously studied precipitation kinetics of Cu-rich precipitates [8]. There are some similarities and some differences in the present Au-rich precipitation and the previously studied Cu-rich precipitation. For Cu-rich precipitates nucleation can take place within the Fe matrix in the absence of dislocations, but it is found to be significantly promoted by the presence of these dislocations [8]. For Au-rich precipitates nucleation in the Fe matrix can only take place in the presence of dislocations and is promoted by a higher dislocation density [9]. This difference in behaviour originates from the size difference between the solute atom and the Fe matrix atom, which is small for Cu and large for Au. The relative difference in atomic volume corresponds to a volume strain of: $\varepsilon_v = 0.3\%$ for Cu ($r_{Cu}/r_{Fe} = 1.001$) and $\varepsilon_v = 44\%$ for Au ($r_{Au}/r_{Fe} = 1.13$). The strain energy strongly affects the effective driving force for nucleation, as it reduces the chemical driving force. The volumetric strain energy can be estimated as: $G_{strain} = (1/2)B(\varepsilon_v)^2$, where B is the bulk modulus ($B = 166$ GPa for bcc Fe [46]). In molar units ($V_{mol} = 7.09$ cm^3/mol for bcc Fe) this results in $G_{strain} = 5 \times 10^{-3}$ kJ/mol for Cu in bcc Fe and $G_{strain} = 115$ kJ/mol for Au in bcc Fe. This clearly illustrates the influence of the atomic size difference on the nucleation process of Cu-rich and Au-rich precipitates in the Fe matrix. As the strain energy for Au-rich precipitation is significant it requires the presence of a dislocation to lower it before nucleation can take place. For the nucleation of Fe_2 W precipitates in the Fe matrix the situation is more complex. The relative difference in atomic volume corresponds to a volume strain of: $\varepsilon_v = 34$ % for W ($r_W/r_{Fe} = 1.10$). This indicates that nucleation of W-rich precipitates is significantly more difficult than for Cu-rich precipitates. As the Fe_2 W precipitate and the Fe matrix have a different lattice structure, additional interfacial strains will contribute to strain energy required for nucleation of the precipitates.

Cold rolling was only applied to introduce preferred nucleation sites for the Au-rich and W-rich precipitates in the form of an enhanced dislocation density. The presence of these dislocations is confirmed in the TEM images of Figs. 1-3. Their influence on the nucleation and growth kinetics Au-rich precipitates is clearly demonstrated in a previous SANS experiment on the Fe-Au alloy with different levels (0 %, 8 % and 24 %) of tensile deformation prior to the aging at 550 °C [9]. It was clearly demonstrated that no significant Au-rich precipitation was observed without deformation and that the transformation kinetics was significantly enhanced when the tensile deformation was enhanced from 8 % to 24 %, indicating that the nucleation rate is enhanced by a higher dislocation density. From an average experimental dislocation cel size of about 100 nm (Figs. 1-3) a dislocation density of $\rho_d \approx 10^{14}$ m^{-2} is estimated for the 20 % rolling reduction.

In previous creep studies on the Fe-Au-W system it was found that both Au-rich precipitation and Fe_2 W precipitation take place during aging at a temperature of 550 °C [20,21]. These studies were conducted under constant stress levels ranging from 170 to 235 MPa and life times from 50 to 225 h. In these studies it was found that Au-rich precipitation was faster than Fe_2 W precipitation. In the present study precipitation aging was monitored in pre-deformed samples during aging for 12 h at temperatures ranging from 650 to 700 °C. These temperatures are higher, but the time scales are shorter and the stress is not present during the aging. The probed time scale of 12 h is apparently not long enough to see a significant amount of Fe_2 W precipitation.

4. Conclusions

In-situ time-resolved SANS experiments were conducted on homogenised cold-rolled ternary Fe-Au-W alloys during aging for 12 h at temperatures of 650 to 700 °C in order to study the kinetics of the nanoscale precipitation. For comparison the precipitation kinetics in the binary counterparts Fe-Au and Fe-W alloys were also studied at an aging temperature of 650 °C. The main conclusions are:

1. During 12 h of aging at 650 °C nanoscale Au-rich precipitates were observed in the Fe-Au-W and Fe-Au alloys by both TEM and SANS. No significant W-rich precipitation was observed in the Fe-Au-W and Fe-W alloys for aging times up to 12 h at 650 °C.
2. The SANS pattern of the cold-rolled Fe-Au-W alloy after 12 h of aging at 650 to 700 °C clearly reveals a preferred orientation for the plate-shaped nanoscale Au-rich precipitates. As these Au-rich precipitates have a fixed orientation relation with the matrix lattice, this preferred orientation originates from texture of the *bcc* matrix grains. This texture has been confirmed by XRD pole figure measurements. A data analysis strategy has been developed that includes the effect of texture and provides both the nuclear and the magnetic SANS separately. As the magnetic SANS is dominant, this contribution is used to study the precipitation kinetics of the Au-rich precipitates.
3. The precipitation kinetics for the plate-shaped Au-rich precipitates is comparable for the ternary Fe-Au-W alloy and the binary Fe-Au alloy. This indicates that the solute W has a negligible effect on the nucleation and growth of the Au-rich precipitates.
4. The temperature dependence of the precipitation kinetics of the Au-rich precipitates in the Fe-Au-W alloy was studied for varying aging at temperatures of 650, 675 and 700 °C. Increasing the temperature results in a faster kinetics and a lower final precipitate fraction. This is expected as the solute diffusivity of Au in an Fe-based *bcc* matrix increases with temperature and the equilibrium phase fraction reduces with temperature in the Fe-Au-W alloy.
5. The present SANS experiments in Fe-Au and Fe-Au-W alloys at aging temperatures from 650 to 700 °C show a faster Au-rich precipitation kinetics compared to the previously investigated in Fe-Au alloys at an aging temperature of 550 °C. The precipitate nucleation at dislocations introduced by cold rolling is found to be effectively instantaneous at the start of the aging process. The amount of Fe present in the Au-rich precipitates is significantly higher with 40 at.% Fe at 650 °C compared to 20 at.% Fe at 550 °C.

CRediT authorship contribution statement

Y. Fu: Investigation, Writing – original draft. **J. Kohlbrecher:** Investigation. **F.D. Tichelaar:** Investigation. **R.W.A. Hendrikx:** Investigation. **A.J. Böttger:** Investigation. **E. Brück:** Supervision, Writing – review & editing. **S. van der Zwaag:** Supervision, Writing – review & editing. **N.H. van Dijk:** Conceptualization, Investigation, Supervision, Writing – review & editing.

Declaration of competing interest

The authors declare that they have no known competing financial interests or personal relationships that could have appeared to influence the work reported in this paper.

Acknowledgments

We thank Kees Kwakernaak for providing the SEM facilities. Fu acknowledges the financial support provided by the China Scholarship Council (CSC). This work is based on experiments performed at the Swiss spallation neutron source SINQ, Paul Scherrer Institute, Villigen, Switzerland. For the TEM results, we acknowledge support from the Kavli Institute of Nanoscience, Delft University of Technology, and the Netherlands Electron Microscopy Infrastructure (NEMI), project number 184.034.014, part of the National Roadmap and financed by the Dutch Research Council (NWO).

Supplementary materials

Supplementary material associated with this article can be found, in the online version, at doi:10.1016/j.mtla.2024.102322.

References

[1] M. Taneike, F. Abe, K. Sawada, Creep-strengthening of steel at high temperatures using nano-sized carbonitride dispersions, Nature 424 (2003) 294–296.
[2] Z.B. Jiao, J.H. Luan, M.K. Miller, C.T. Liu, Precipitation mechanism and mechanical properties of an ultra-high strength steel hardened by nanoscale NiAl and Cu particles, Acta Mater. 97 (2015) 58–67.
[3] S. Jiang, H. Wang, Y. Wu, X. Liu, H. Chen, M. Yao, B. Gault, D. Ponge, D. Raabe, A. Hirata, M. Chen, Y. Wang, Z. Lu, Ultrastrong steel via minimal lattice misfit and high-density nanoprecipitation, Nature 544 (2017) 460–465.
[4] K. Laha, J. Kyono, S. Kishimoto, N. Shinya, Beneficial effect of B segregation on creep cavitation in a type 347 austenitic stainless steel, Scr. Mater. 52 (2005) 675–678.
[5] M.D. Hager, P. Greil, C. Leyens, S. van der Zwaag, U.S. Schubert, Self-healing materials, Adv. Mater. 22 (2010) 5424–5430.
[6] N. van Dijk, S. van der Zwaag, Self-healing phenomena in metals, Adv. Mater. Interfaces 5 (2018) 1800226.
[7] M. Arseenko, F. Hannard, L. Ding, L. Zhao, E. Maire, J. Villanova, H. Idrissi, A. Simar, A new healing strategy for metals: programmed damage and repair, Acta Mater. 238 (2022) 118241.
[8] S.M. He, N.H. van Dijk, M. Paladugu, H. Schut, J. Kohlbrecher, F.D. Tichelaar, S. van der Zwaag, *In situ* determination of aging precipitation in deformed Fe-Cu and Fe-Cu-B-N alloys by time-resolved small-angle neutron scattering, Phys. Rev. B 82 (2010) 174111.
[9] S. Zhang, J. Kohlbrecher, F.D. Tichelaar, G. Langelaan, E. Brück, S. van der Zwaag, N.H. van Dijk, Defect-induced Au precipitation in Fe-Au and Fe-Au-B-N alloys studied by *in situ* small-angle neutron scattering, Acta Mater. 61 (2013) 7009–7019.
[10] S. Zhang, C. Kwakernaak, W.G. Sloof, E. Brück, S. van der Zwaag, N.H. van Dijk, Self healing of creep damage by gold precipitation in iron alloys, Adv. Eng. Mater. 17 (2015) 598–603.
[11] S. Zhang, K. Kwakernaak, F.D. Tichelaar, W.G. Sloof, M. Kuzmina, M. Herbig, D. Raabe, E. Brück, S. van der Zwaag, N.H. van Dijk, Autonomous Repair Mechanism of Creep Damage in Fe-Au and FeAuBN Alloys, Metall. Mater. Trans. A 46A (2015) 5656–5670.
[12] S. Zhang, H. Fang, M.E. Gramsma, C. Kwakernaak, W.G. Sloof, F.D. Tichelaar, M. Kuzmina, M. Herbig, D. Raabe, E. Brück, S. van der Zwaag, N.H. van Dijk, Autonomous filling of grain-boundary cavities during creep loading in FeMo alloys, Metall. Mater. Trans. A 47A (2016) 4831–4844.
[13] H. Fang, C.D. Versteylen, S. Zhang, Y. Yang, P. Cloetens, D. Ngan-Tillard, E. Brück, S. van der Zwaag, N.H. van Dijk, Autonomous filling of creep cavities in Fe-Au alloys studied by synchrotron Xray nano-tomography, Acta Mater. 121 (2016) 352–364.
[14] H. Fang, N. Szymanski, C.D. Versteylen, P. Cloetens, C. Kwakernaak, W.G. Sloof, F. D. Tichelaar, S. Balachandran, M. Herbig, E. Brück, S. van der Zwaag, N.H. van Dijk, Self healing of creep damage in iron-based alloys by supersaturated tungsten, Acta Mater. 166 (2019) 531–542.
[15] E. Hornbogen, The role of strain energy during precipitation of copper and gold from alpha iron, Acta Metall. 10 (1962) 525–533.
[16] E. Hornbogen, Guinier-Preston zones in b.c.c. iron, Acta Metall. 10 (1962) 1187–1189.
[17] J. Higgins, P. Wilkes, Precipitation in the Fe-Mo and Fe-Au systems, Philos. Mag. 25 (1972) 599–623.
[18] G. Marchal, P. Mangin, C. Janot, Crystal growth and precipitation in thin films of amorphous Fe-Au alloys, Philos. Mag. 32 (1975) 1007–1021.
[19] Y. Liu, Y. Ge, D. Yu, Thermodynamic descriptions for Au–Fe and Na–Zn binary systems, J. Alloys Comp. 476 (2009) 79–83.
[20] Y. Fu, C. Kwakernaak, W.G. Sloof, F.D. Tichelaar, E. Brück, S. van der Zwaag, N. H. van Dijk, Competitive healing of creep-induced damage in a ternary Fe-3Au-4W alloy, Metall. Mater. Trans. A 51A (2020) 4442–4455.
[21] Y. Fu, H. Fang, F. Monaco, P. Cloetens, C. Kwakernaak, F.D. Tichelaar, J.G. van Meel, E. Brück, S. van der Zwaag, N.H. van Dijk, Self healing of creep-induced damage in Fe-3Au-4W by multiple healing agents studied by synchrotron X-ray nano-tomography, Acta Mater. 239 (2022) 118266.
[22] G. Kostorz, Small-angle scattering studies of phase separation and defects in inorganic materials, J. Appl. Cryst. 24 (1991) 444–456.
[23] P. Fratzl, Small-angle scattering in materials science - a short review of applications in alloys, ceramics and composite materials, J. Appl. Cryst. 36 (2003) 397–404.
[24] A. Wiedenmann, in: T. Chatterji (Ed.), Elsevier, Amsterdam, 2006, p. 473.
[25] E. Eidenberger, R. Schnitzer, G.A. Zickler, M. Schober, M. Bischof, P. Staron, H. Leitner, A. Schreyer, H. Clemens, Application of photons and neutrons for the characterization and development of advanced steels, Adv. Eng. Mater. 13 (2011) 664–673.
[26] F. De Geuser, A. Deschamps, Precipitate characterisation in metallic systems by small-angle X-ray or neutron scattering, C. R. Phys. 13 (2012) 246–256.
[27] L. Karge, D. Lang, J. Schatte, R. Gilles, S. Busch, P. Leibenguth, H. Clemens W. Petry, Characterization of anisotropic pores and spatially oriented precipitates in sintered Mo-base alloys using small-angle neutron scattering, J. Appl. Cryst. 51 (2018) 1706–1714.
[28] C. Ioannidou, A. Navarro-López, R.M. Dalgliesh, A. Rijkenberg, X. Zhang, B. Kooi, N. Geerlofs, C. Pappas, J. Sietsma, A.A. van Well, S.E. Offerman, Phase-transformation and precipitation kinetics in vanadium micro-alloyed steels by *in-situ*, simultaneous neutron diffraction and SANS, Acta Mater. 220 (2021) 117317.
[29] J. Kohlbrecher, W. Wagner, The new SANS instrument at the Swiss spallation source SINQ, J. Appl. Cryst. 33 (2000) 804–806.
[30] https://www.psi.ch/en/sinq/sansi/bersans 2024.
[31] https://www.sasview.org/ 2024.
[32] A.S. Arrott, B. Heinrich, Application of magnetization measurements in iron to high temperature thermometry, J. Appl. Phys. 52 (1981) 2113–2115.
[33] L.A. Feigin, D.I. Svergun, Structure Analysis by Small-Angle X-Ray and Neutron Scattering, Springer, New York, 1987.
[34] J.S. Pedersen, Analysis of small-angle scattering data from colloids and polymer solutions: modeling and least-squares fitting, Adv. Colloid Interface Sci. 70 (1997) 171–210.
[35] P. Lindner, S. Hess, Analysis of structural anisotropy from SANS-multidetector data, Phys. B 156157 (1989) 512–514.
[36] C.D. Versteylen, N.H. van Dijk, M.H.F. Sluiter, First-principles analysis of solute diffusion in dilute bcc Fe-X alloys, Phys. Rev. B 96 (2017) 094105.
[37] W.A. Johnson, K.F. Mehl, Reaction kinetics in processes of nucleation and growth, Trans. Am. Inst. Min. (Metall.) Eng. 135 (1939) 416–442.
[38] M. Avrami, Kinetics of phase change. I. General theory, J. Chem. Phys. 7 (1939) 1103–1112.
[39] M. Avrami, Kinetics of phase change. II. Transformation-time relations for random distribution of nuclei, J. Chem. Phys. 8 (1940) 212–224.
[40] M. Avrami, Kinetics of phase change. III. Granulation, phase change, and microstructure, J. Chem. Phys. 9 (1941) 177–184.
[41] A.N. Kolmogorov, Izv. Acad. Nauk. SSSR 3 (1937) 355–359.
[42] G. Laplanche, S. Berglund, C. Reinhart, A. Kostka, F. Fox, E.P. George, Phase stability and kinetics of s-phase precipitation in CrMnFeCoNi high-entropy alloys, Acta Mater. 161 (2018) 338–351.
[43] G. Laplanche, Growth kinetics of σ-phase precipitates and underlying diffusion processes in CrMnFeCoNi high-entropy alloys, Acta Mater. 199 (2020) 193–208.
[44] H.I. Aaronson, M. Enomoto, J.K. Lee, Mechanisms of Diffusional Phase Transformations in Metals and Alloys, CRC Press, Boca Raton, USA, 2010.
[45] Z.W. Zhang, C.T. Liu, X.-L. Wang, K.C. Littrell, M.K. Miller, K. An, B.A. Chin, From embryos to precipitates: a study of nucleation and growth in a multicomponent ferritic steel, Phys. Rev. B 84 (2011) 174114.
[46] J.J. Adams, D.S. Agosta, R.G. Leisure, H. Ledbetter, Elastic constants of monocrystal iron from 3 to 500 K, J. Appl. Phys. 100 (2006) 113530.